AIAA JOURNAL
Vol. 44, No. 11, November 2006

Unsteady and Transitional Flows Behind Roughness Elements

F. Gökhan Ergin* and Edward B. White†
Case Western Reserve University, Cleveland, Ohio 44106

The role of surface roughness in boundary layers continues to be a topic of significant interest, especially with regard to how controlled roughness might be used to delay laminar-to-turbulent transition. Although it may be useful for control, large-amplitude roughness may itself lead to transition. In an effort to understand the breakdown mechanics associated with large-amplitude surface roughness, experiments are conducted to investigate the steady and unsteady disturbances generated by three-dimensional roughness elements whose amplitudes are close to the critical roughness-based Reynolds number Re_k for roughness-induced transition. Measurements are obtained in a flat-plate boundary layer downstream of a spanwise array of cylindrical roughness elements at both subcritical and supercritical values of Re_k. The steady disturbance field has strong shear in the wall-normal and spanwise directions, and the unsteady streamwise velocities in the roughness elements' wake show evidence of hairpin vortices. The locations of maximum fluctuation intensity correspond to the locations of inflection points in the steady flow streamwise velocity, and this suggests that the fluctuations may result from a Kelvin–Helmholtz-type instability. Temporal power spectra indicate an unstable band of frequencies from 300 to 800 Hz. The Strouhal number associated with the 650-Hz fluctuations that are often observed to be the strongest give $Sr = 0.15$, a value that is in good agreement with previous findings. At supercritical Re_k, rapid transition takes place when the unsteady disturbances reach nonlinear amplitudes. The disturbance growth rates indicate that in this situation transition can be understood as a competition between the unsteady disturbance growth and the rapid relaxation of the steady flow that tends to stabilize these disturbances.

Nomenclature

D	=	roughness diameter
E	=	steady disturbance energy
e_f	=	unsteady disturbance energy in a frequency band centered at f
f	=	frequency
H	=	shape factor, δ^*/θ
k	=	roughness height
N	=	number of samples
Re_k	=	roughness-based Reynolds number, $\bar{U}(k)k/\nu$
Re'	=	unit Reynolds number, U_∞/ν
Sr	=	Strouhal number of unsteady vortex shedding, $f\delta^*/U_\infty$
$\bar{U}$	=	spanwise-invariant streamwise basic state velocity
U'	=	steady streamwise disturbance velocity
U_∞	=	freestream velocity
u'	=	unsteady streamwise disturbance velocity
x, y, z	=	streamwise, wall-normal, and spanwise coordinates
x_k	=	streamwise location of the roughness array
α	=	spatial growth rate
δ	=	boundary-layer length scale, $[(x - x_{\text{vle}})/Re']^{1/2}$
δ^*	=	displacement thickness
λ_k	=	roughness spacing
η	=	Blasius coordinate, y/δ
θ	=	momentum thickness
ν	=	kinematic viscosity

Subscripts

c	=	centerline
crit	=	critical
rms	=	root-mean-square
s	=	shedding
samp	=	sampling
vle	=	virtual leading edge

Received 30 April 2005; revision received 11 October 2005; accepted for publication 12 October 2005.

*Postdoctoral Research Associate, Department of Mechanical and Aerospace Engineering. Member AIAA.

†Assistant Professor, Department of Mechanical and Aerospace Engineering. Senior Member AIAA.

I. Introduction

THE study of laminar-to-turbulent transition on surfaces with significant roughness levels has had a long history motivated by the need to understand transition on realistic surfaces. Laboratory studies on low-speed flows have tended to treat three main classes of roughness: two-dimensional roughness strips; three-dimensional, isolated roughness elements or arrays of three-dimensional elements; and random distributed three-dimensional roughness fields. The distinctions among these arise from how each is accommodated as a disturbance source in stability theory and from practical considerations of what actually exists on aerodynamic surfaces.

In two-dimensional boundary layers, the role of two-dimensional roughness is well understood as a generator of two-dimensional Tollmien–Schlichting (TS) waves. Goldstein[1] uses a triple-deck analysis to show that the streamwise variations of the mean flow that are produced by two-dimensional roughness scatter acoustic waves into TS wavelengths and, thus, provide a receptivity mechanism for unstable TS waves. Additional details on the receptivity of TS waves are in the review by Saric et al.[2] Because the TS-wave amplitudes depend on the roughness amplitude, increasing the roughness amplitude should be expected to move gradually the transition location toward the two-dimensional roughness, and this is exactly what was observed in numerous transition experiments of the 1940s and 1950s.[3,4]

The role of isolated and distributed three-dimensional roughness in two-dimensional boundary layers has not been as well understood on a theoretical basis because the stationary, spanwise varying disturbances created by three-dimensional roughness are not unstable within the context of a normal-mode stability analysis.[5] Typically, transition in the wake of isolated three-dimensional roughness elements is predicted using correlations based on a critical roughness-based Reynolds number $Re_{k,\text{crit}}$, established in the 1950s.[4,6–10] Within the context of the correlation approach, if a roughness element exceeds Reynolds number $Re_{k,\text{crit}}$, then transition is expected to occur at or just aft of the roughness element, but if the critical value is not exceeded, then no effect is expected.

The correlation approach based on a critical Reynolds number Re_k is well established, but provides no guidance on the more subtle

effects that subcritical three-dimensional roughness can have on the behavior of a laminar boundary layer. In particular, the recent development of transient growth theory indicates that whereas the steady disturbances produced by subcritical roughness elements are stable in the context of traditional linear stability theory for modal, that is, exponentially growing or decaying, disturbances there can be a brief period of algebraic growth of the steady disturbances that could, potentially, lead to transition.[5,11] Moreover, the optimal transient disturbances, those that undergo the largest growth over a specified distance or time, are steady, spanwise-varying disturbances,[12–15] exactly the type of disturbance that is produced by three-dimensional roughness elements. This provides a renewed impetus for examining the role of three-dimensional roughness elements as a potential source of transient disturbances and bypass transition.[5] White and Reshotko,[16] White,[17] White and Ergin,[18] and White et al.[19] have addressed this question experimentally and have verified that isolated three-dimensional roughness elements do generate stationary disturbances that undergo transient growth but that some details of this growth is not well described by optimal-disturbance theory.

With regard to the subtle effects that subcritical three-dimensional roughness can play in a laminar boundary layer, a particularly interesting recent finding by Cossu and Brandt[20,21] is that stationary, finite-amplitude optimal disturbances can suppress the growth of TS-like disturbances in a boundary layer. In Cossu and Brandt's numerical studies, spanwise-invariant disturbances in the TS-unstable frequency band are introduced into a boundary layer that is modulated by stationary, spanwise-periodic optimal disturbances. As the amplitude of the transient disturbances is increased, the unsteady TS-like disturbances become increasingly modulated in the spanwise direction and experience progressively slower growth in the streamwise direction. Once the amplitude of the transient disturbances reaches about 20% of U_∞ at their maximum-growth location, the unsteady disturbance growth is completely suppressed. The implication is that it may be possible to use spanwise arrays of three-dimensional roughness elements to delay passively or suppress TS-dominated transition. This control approach would be similar in appearance to the crossflow-dominated transition control approach using subcritically spaced roughness elements developed by Saric et al.,[22] but would be quite different in terms of the instability mechanisms involved.

Implementing the control approach inspired by Cossu and Brandt's[20,21] calculations involves introducing the largest possible stationary transient disturbances because as the amplitudes of the transient disturbances are increased there is progressively less TS growth. However, one means of introducing stationary disturbances, placing arrays of three-dimensional roughness elements on the surface, will itself lead to transition if the amplitudes of the roughness elements exceed Reynolds number $Re_{k,\mathrm{crit}}$. Another danger is that the stationary transient disturbances may become unstable to a high-frequency secondary instability once their amplitude exceeds 26% of U_∞ (Ref. 23). Therefore, there is considerable uncertainty as to whether the control approach is feasible.

In an effort to better understand the limitations on implementing Cossu and Brandt's control approach, the experiment presented here investigates the mechanisms associated with the transient growth of stationary disturbances and the rapid transition to turbulence associated with large-amplitude three-dimensional roughness elements. The focus is on obtaining detailed measurements of the steady and unsteady flow in the elements' wakes. These data are used to identify the mechanism associated with immediate transition and to determine what role, if any, transient growth of stationary disturbances or the secondary instability of these disturbances may play in this transition scenario. In the following sections, a brief review of the literature on the role of isolated three-dimensional disturbances is presented, the experimental facility and approach are explained, and the experimental results are presented and discussed.

II. Review of Experiments on Isolated Surface Roughness Effects

The role of isolated three-dimensional roughness elements was initiated in the 1950s by the flow visualization studies of Gregory and Walker,[24] who established a basic understanding of the horseshoe and hairpin vortex structure that exists around a moderate-to-large-amplitude roughness element in a boundary layer. Gregory and Walker's results have been enhanced by numerous other flow-visualization studies that culminate with the experiments of Acarlar and Smith.[25] These lead to the conclusion that the topology of the flow about an isolated three-dimensional roughness element in a boundary layer consists of a steady horseshoe vortex that wraps around the upstream side of an isolated roughness element and trails two steady counter-rotating legs downstream. The sense of rotation is such that along the line directly behind the roughness element the vertical velocity induced by the vortices is directed down toward the surface. At sufficiently high values of Reynolds number Re_k, unsteady hairpin vortices originate periodically from the separated region just aft of the roughness element. The heads of these vortices move up and away from the roughness element and are convected downstream. Acarlar and Smith show that shedding originates from hemispherical roughness elements at around $Re_k \approx 120$ and that a Strouhal number based on the shedding frequency, roughness height, and the velocity at the roughness height, $Sr = fk/\bar{U}(k)$, increases from below 0.05 at the lowest Reynolds number Re_k values that produce shedding to values between 0.2 and 0.4 as Re_k exceeds 1200 (Ref. 25). Hot-wire measurements by Klebanoff et al.[26] give similar results, but Klebanoff et al. cast their data in terms of a Strouhal number based on displacement thickness, $Sr = f\delta^*/\bar{U}(k)$ and find that $Sr \approx 0.3$ from $Re_k = 300$ to 1700 for hemispherical roughness elements. Klebanoff et al. further find that cylindrical elements with $D = k$ are found to produce somewhat lower Strouhal numbers that increase slightly from $Sr \approx 0.2$ at $Re_k = 400$ to $Sr \approx 0.25$ at $Re_k = 1200$.

With regard to critical Reynolds number $Re_{k,\mathrm{crit}}$, the critical roughness-based Reynolds number for immediate roughness-induced transition, the general finding is that the effect of isolated three-dimensional roughness elements is "more critical" than two-dimensional roughness strips. By more critical, it is meant that as critical Reynolds number $Re_{k,\mathrm{crit}}$ is exceeded the transition location moves forward very rapidly but that below critical Reynolds number $Re_{k,\mathrm{crit}}$, an isolated three-dimensional element has little or no effect on transition.[4,6–10] This is quite different than the behavior of boundary layers with two-dimensional roughness that tend to show transition gradually moving forward with increasing Reynolds number Re_k. Studies originating with those by Klebanoff et al.[27] establish that critical Reynolds number $Re_{k,\mathrm{crit}}$ lies between 600 and 900 for isolated elements whose height-to-diameter ratio is approximately unity. The most recent and detailed studies of critical Reynolds number $Re_{k,\mathrm{crit}}$ are also by Klebanoff et al.,[26] who find somewhat lower values of critical Reynolds number $Re_{k,\mathrm{crit}}$ than previous studies (e.g., Ref. 28) but have a somewhat less-stringent definition of transition. A key finding in Ref. 26 is that even at limiting cases of high Reynolds number Re_k, there is always a finite distance between the roughness element and the resulting turbulent flow. The implication is that, at high values of Reynolds number Re_k, transition occurs as the result of an instability of the distorted, reversed flow in the roughness element's wake that requires some finite distance to develop. Other key findings of the early transition correlation work are that critical Reynolds number $Re_{k,\mathrm{crit}}$ scales roughly as $(k/D)^{2/5}$, meaning that transition occurs for progressively lower critical Reynolds number $Re_{k,\mathrm{crit}}$ values as the roughness diameter is increased[4,9] and that elements in spanwise arrays behave as isolated elements when their spacing is three times their diameter or larger.[9]

Although transition correlations are useful, they do not reveal the detailed mechanism for transition, nor do they assist in designing transition control strategies besides simply placing design limits on acceptable roughness levels. Understanding the mechanisms requires detailed flow studies that can be used in conjunction with stability theories. However, there have been relatively few studies of the detailed flowfield in the wake of isolated roughness elements that can be used to inspire or validate mechanisms-based theories. Notable exceptions among the early literature are by Mochizuki,[29] Tani et al.,[28] Kendall,[30] and Klebanoff et al.[26] Recent measurements by White and Ergin,[18] White et al.,[19] and White and Ergin[31] on the

receptivity of transient disturbances to surface roughness provide additional data. All of these studies find complicated distortions of the steady flow in the roughness elements' wakes. Just aft of a roughness element in what Kendall[30] refers to as the near-wake region, the flow is decelerated in the $x-y$ (streamwise–wall-normal) plane that passes through the roughness element's center. However, farther downstream, the velocities in this plane can become accelerated with decelerated velocities on either side of the centerline plane. For this far-wake region, the finding is that if the roughness element is not sufficiently large to cause transition the velocity excess can grow slightly but eventually decays.

In the context of the developing understanding of transient growth, what occurs when Reynolds number Re_k is below critical Reynolds number $Re_{k,\mathrm{crit}}$ is that the roughness elements produce a large initial disturbance that may be quite different than an optimal disturbance.[19] This disturbance includes decelerated profiles directly behind the roughness element[19,30,31] and the energy of this disturbance decays rapidly for a short distance (Kendall's near wake). Farther downstream, some transient growth occurs that may or may not be significant relative to the disturbance's initial amplitude[19] (Kendall's far wake). The transient growth results from the integrated effect of the stationary horseshoe vortex that redistributes streamwise momentum across the shear layer. This is the lift-up mechanism described by Landahl[32] in an early paper on transient growth. Tumin and Reshotko[33] have found that, although roughness-induced disturbances are not optimal,[17,19] the growth from the location of minimum disturbance energy that separates the near wake from the far wake is similar to optimal growth.

Vortex shedding in the wake of moderate-to-large-amplitude elements supports the notion that transition beyond critical Reynolds number $Re_{k,\mathrm{crit}}$ is due to an instability of the elements' distorted wake flow. However, there are only a few studies that correlate the fluctuation intensities to particular locations in the wake. One of these is a series of u'_{rms} measurements by Klebanoff et al.[26] in the near wake of a hemispherical roughness element. The measurements were obtained across a range of span locations for various heights in the boundary layer. High in the boundary layer, there is a single peak of u'_{rms} centered at the roughness location, whereas lower in the boundary layer, there are two peaks that are located on either side of the roughness centerline. These results hint at a complicated instability associated with the various features of the distorted wake flow.

The main objective of the present work is to link the steady and unsteady disturbance fields and to use this link to reveal the instability mechanism whose existence is suggested by the data obtained by Klebanoff et al.[26] The hope is that a detailed understanding of this mechanism will lead to an improved sense of why critical Reynolds number $Re_{k,\mathrm{crit}}$ values are what they are and how large-amplitude transient disturbances may be created for TS-suppression purposes.

III. Experiments and Data Analysis

The experiments closely follow the previous work by White and coworkers and Reshotko,[16] White,[17] White and Ergin,[18] and White et al.[19] in terms of experimental setup. The facility used for the experiments is the Case Wind Tunnel, an open-return facility with a $0.71 \times 0.71 \times 2.7\ \mathrm{m}^3$ test section and a maximum operation speed of 25 m/s. The test section features an externally mounted, computer-controlled hot-wire traverse mechanism with microstepping motors that move hot-wire sensors in three perpendicular directions with micrometer-step resolution. Restricted to a high-pass frequency of 1 Hz, the turbulent u'_{rms} level is 0.05% of U_∞.

Measurements are obtained in the boundary layer of a 9.5-mm-thick aluminum flat plate that is polished to a near-mirror finish. The plate has a 25-mm-long elliptical leading edge, and the stagnation streamline is controlled by a 300-mm-long trailing-edge flap. The boundary layer's virtual leading-edge location and the effective unit Reynolds number and error estimates for these quantities are generated using the Levenberg–Marquardt algorithm (see Ref. 34) to perform nonlinear least-squares fit to the boundary layer's displacement and momentum thicknesses as a function of streamwise position. At the experiments' nominal freestream speed of 12.2 m/s, the unit Reynolds number is $Re' = 764 \times 103\ \mathrm{m}^{-1}$, and the virtual leading edge location is $x_{\mathrm{vle}} = -7$ mm (upstream of the physical leading edge). Great care is exercised in the alignment of the flat plate, which is essential to ensure a zero-pressure-gradient flow. Measurements show that the mean shape factor is $H = 2.56$, so that the flow is slightly accelerated but within an acceptable deviation of the zero-pressure-gradient value, $H = 2.59$ (Ref. 35).

Disturbances are generated by a spanwise array of cylindrical roughness elements located 300 mm down-stream of the plate's physical leading edge. Roughness arrays are used because they generate controlled disturbance inputs and permit the use of various data-reduction techniques, especially spatial phase-locked averaging, that greatly improve the signal-to-noise characteristics of the data. The roughness elements consist of 6.35-mm-diam, 102-μm-thick adhesive-backed paper labels that are stacked to provide desired roughness heights. Seven, eight, or nine layers are used to provide Reynolds number Re_k values of 202, 264, and 334, respectively. These Re_k values span a range from subcritical to supercritical and reveal the differences between unsteady fluctuations that do and do not lead to roughness-induced transition in the elements' near wake. Based on the k/D values of these three roughness heights, critical Reynolds number $Re_{k,\mathrm{crit}}$ is expected to lie between 250 and 275. Rice[36] has previously observed roughness-induced breakdown in the Case wind tunnel under similar conditions at $Re_k = 254$.

It is notable that results of a recent simulation of this experiment by Rizzetta and Visbal[37] are more consistent with what would be expected had the experiments featured Re_k values of 148, 202, and 264. These values correspond to what would have existed with six, seven, or eight paper layers. Furthermore, using these lower Re_k values leads to improved comparisons between some aspects of the simulation and experimental results. Experiments are currently underway to resolve the discrepancies.

The roughness elements are spaced $\lambda_k = 3D = 19$ mm apart in the spanwise z direction. This spacing is chosen because it affords the greatest number of elements within the spanwise range accessible by the hot-wire traverse while maintaining sufficient distance between the roughness elements that they can be considered to act as isolated roughness elements in the near-wake region.[9] This spacing puts 8 elements within reach of the traverse; the entire array consists of 12 elements to ensure that spanwise periodicity is maintained beyond the traverse's range. The flat plate's leading edge and the roughness array are shown in Fig. 1.

The hot-wire measurements of the streamwise velocity's steady and unsteady components are obtained in planes perpendicular to the flow direction. A pair of single-element hotwire sensors oriented perpendicular to the flow are used to measure simultaneously the boundary-layer and freestream velocities. In each measurement plane, the spanwise movements of the hot-wire probes are constant; the 19-mm spacing is covered in 12 steps. The wall-normal step is variable with 400-μm steps outside the boundary layer (starting at approximately $\eta = 8$), and progressively smaller steps are used within the boundary layer. Once a cutoff velocity is reached, the sensors are moved away from the plate to their original position. This scanning technique is similar to what was used in Ref. 17.

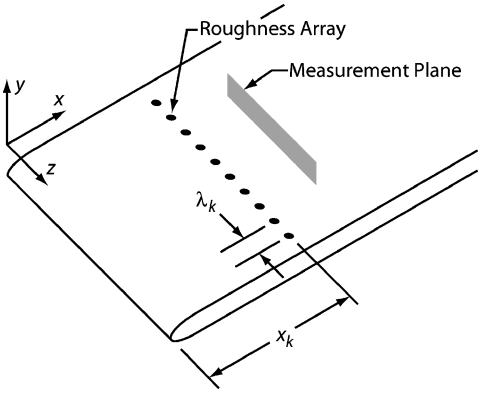

Fig. 1 Schematic of flat plate and roughness array.

However, the wall-location estimation algorithm has been adjusted to avoid errors that affected earlier results.[31]

At each measurement location, the velocity is sampled at 10 kHz. The signal is divided into 1024-point segments, and each segment is Fourier transformed. The number of segments increases from 8 to 12 to 18 as the boundary-layer sensor approaches to the flat surface so that the measurements closest to the wall are well resolved without requiring that all points be sampled as extensively. The average of the individual segments' transforms at each position is computed, and the one-sided, magnitude-averaged, temporal power spectral density (PSD) of that particular measurement location is computed.[34] The PSD normalization is such that an integration of PSD over the frequency domain from $f = 0$ to the Nyquist frequency is equal to u'^2_{rms}, the square of the temporal root-mean-square (rms) of the unsteady velocity fluctuation.

Of interest in this work are the steady disturbances of the Blasius boundary layer that are known to undergo transient growth in the streamwise direction, the unsteady disturbances associated with vortex shedding and roughness-induced transition, and the possible connections between both types of disturbances. To generate a quantitative measure of these disturbances and their growth, the velocity field is separated into three components: the spanwise-invariant basic state $\bar{U}(x, y)$, the spanwise-varying steady disturbance $U'(x, y, z)$, and the unsteady disturbance $u'(x, y, z, t)$. As in Refs. 18, 19, and 31, the spanwise-invariant basic state is not simply the spanwise mean of the steady flow. Instead, it is the mean of the steady velocity profiles obtained at z locations between roughness elements where the flow is most representative of Blasius flow. This approach means that U' includes a contribution due to the spanwise-invariant part of the disturbance. All velocities, $\bar{U}$, U', and u', are made dimensionless using U_∞.

When this velocity decomposition is used, the total disturbance energy associated with the steady disturbances is given by

$$E_{\text{rms}}(x) = \int_{\eta=0}^{\infty} \left[u'_{\text{rms}}(x, \eta)\right]^2 \mathrm{d}\eta$$

where $U'_{\text{rms}}(\eta)$ is the spatial rms U' disturbance obtained along a spanwise line for a particular x, η combination. Similarly, the total disturbance energy associated with the unsteady fluctuations is obtained from the temporal u'_{rms} data using

$$e_{\text{rms}}(x) = \int_{\eta=0}^{\infty} \int_{z=-\frac{1}{2}}^{\frac{1}{2}} [u'_{\text{rms}}(x, \eta, z)]^2 \,\mathrm{d}\eta \,\mathrm{d}z$$

where z is made dimensionless using λ_k. The unsteady disturbance energy of 100-Hz bands centered at $f_0 = 650$ and 1300 Hz (the frequencies that will be of interest later) are computed using

$$e_{f_0}(x) = \int_{\eta=0}^{\infty} \int_{z=-\frac{1}{2}}^{\frac{1}{2}} \int_{f=f_0-\Delta f}^{f_0+\Delta f} \mathrm{PSD}(x, \eta, z, f) \,\mathrm{d}\eta \,\mathrm{d}z \,\mathrm{d}f$$

where $\Delta f = 50$ Hz. The PSD normalization just discussed makes it possible to interpret e_{650} and e_{1300} as fractions of e_{rms}. Because U'_{rms} is generated using data from spanwise lines that extend across eight roughness wavelengths, E_{rms} is representative of the stationary disturbance that exists across the entire spanwise field. However, e_{rms}, e_{650}, and e_{1300} are computed across a single roughness wavelength. The reason for this is that the the unsteady disturbances are somewhat variable from element to element, and therefore, it is most appropriate to consider each separately.

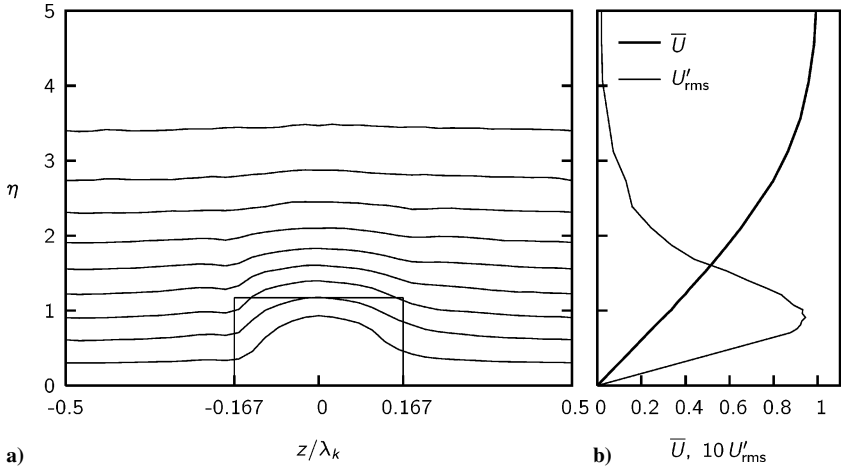

Fig. 2 Steady streamwise flow at $x = 310$ mm for $Re_k = 202$: a) streamwise velocity contours and b) steady flow profiles; ——, 10% increments of U_∞ and box, approximate size and location of roughness element's projection onto η, z plane.

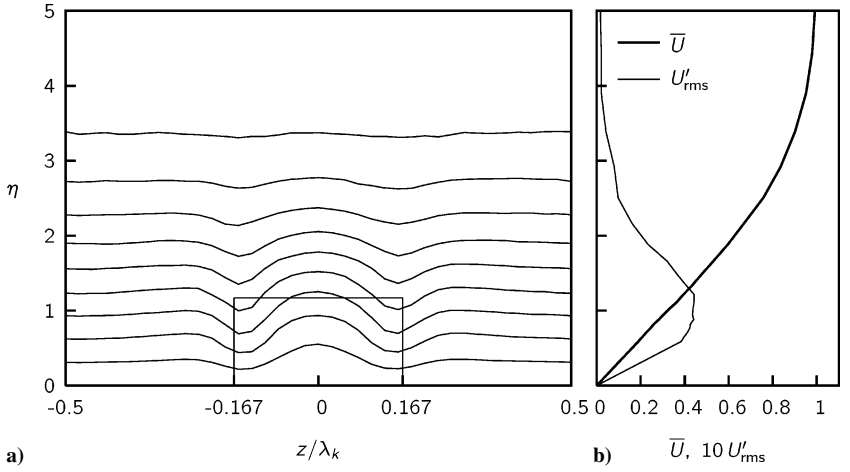

Fig. 3 Steady streamwise flow at $x = 330$ mm for $Re_k = 202$: a) streamwise velocity contours and b) steady flow profiles; ——, 10% increments of U_∞ and box, approximate size and location of roughness element's projection onto η, z plane.

IV. Results and Discussion

The lowest-disturbance configuration for the present work is the roughness configuration with $Re_k = 202$, which is below critical Reynolds number $Re_{k,\mathrm{crit}}$ but is large enough to produce unsteady fluctuations of significant amplitude. The steady flow produced by this roughness array is shown in Figs. 2 and 3, which give the spatially phase-lock averaged steady streamwise velocities at $x = 310$ and 330 mm, respectively. In Figs. 2 and 3, the rectangle in the contour plot indicates the approximate projection of the $Re_k = 202$ roughness element onto the η, z plane. The shape factor given earlier indicates that the $\bar{U}(\eta)$ profiles represented by heavy solid lines are in excellent agreement with the Blasius profile. The two larger-amplitude roughness arrays with $Re_k = 264$ and 334 generate nearly identical $\bar{U}(\eta)$ profiles and $U'_{\mathrm{rms}}(\eta)$ profiles, whose amplitudes scale roughly as Reynolds number Re_k.

The evolution of the steady disturbance energy generated by the three roughness configurations is shown in Fig. 4. In all configurations, the total disturbance energy decreases rapidly just aft of the roughness elements and undergoes transient growth farther downstream. In the $Re_k = 202$ and 264 configurations, the algebraic growth rate decreases with increasing x and, beyond $x = 400$ mm, the total disturbance energy remains roughly constant for the remaining portion of the measurement domain. This behavior is consistent with what is observed in other roughness-induced transient growth experiments.[17–19] However, for $Re_k = 334$, E_{rms} undergoes a second rapid decrease beginning at $x = 425$ mm. This occurs because the roughness is supercritical and trips turbulence. The resulting turbulent mixing reduces the spanwise velocity gradients and, consequentially, the energy of the steady disturbances. The flow is observed to be completely turbulent downstream of $x = 475$ mm.

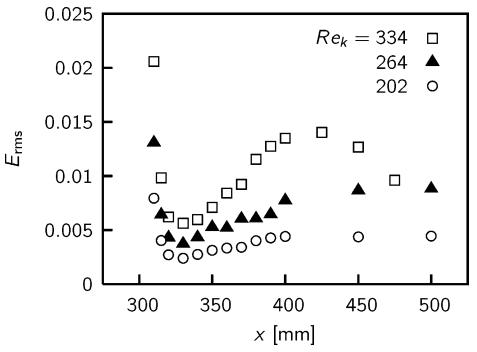

Fig. 4 Streamwise evolution of steady disturbance energy E_{rms}.

A. Nontransitional Configuration, $Re_k = 202$

An understanding of the unsteady disturbances' evolution is obtained by monitoring the downstream evolution of the fluctuation intensity. Figure 5 shows contours of the steady and unsteady streamwise velocities for the $Re_k = 202$ configuration at $x = 310$, 350, 400, and 500 mm. Although data are available behind eight roughness elements, only one-half of the spanwise domain is plotted. The colored contours in Fig. 5 indicate the temporal u'_{rms} velocity fluctuation intensity. (The contour levels follow an exponential distribution so that wide variations in u'_{rms} can be visualized.) The maximum value of u'_{rms} in Fig. 5 is 0.4% of U_∞. Although great attention is given to produce identical roughness elements, there are significant variations among roughness elements' fluctuation intensities. Therefore, the spanwise phase-locked averaging technique is not used for unsteady fluctuation intensities and data in the wake of the second roughness element centered at $z/\lambda_k = -0.5$ will be used for analysis.

In the near wake at $x = 310$ mm, the fluctuations are weak and concentrated mostly in small lobes directly downstream of the roughness elements' centerline ($z/\lambda_k = -1.5, -0.5, 0.5$, and 1.5) around $\eta = 1.5$. Note that these are the locations where the local velocity profile has an inflection point in the η direction, that is,

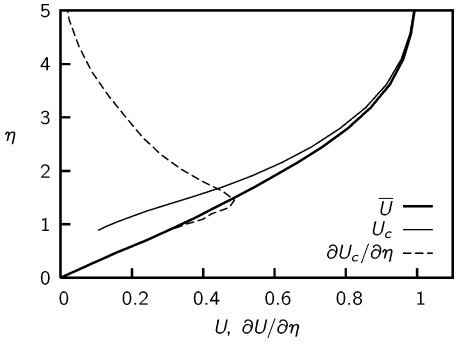

Fig. 6 Basic state, centerline, and $\partial U/\partial\eta$ profiles at $x = 310$ mm for $Re_k = 202$.

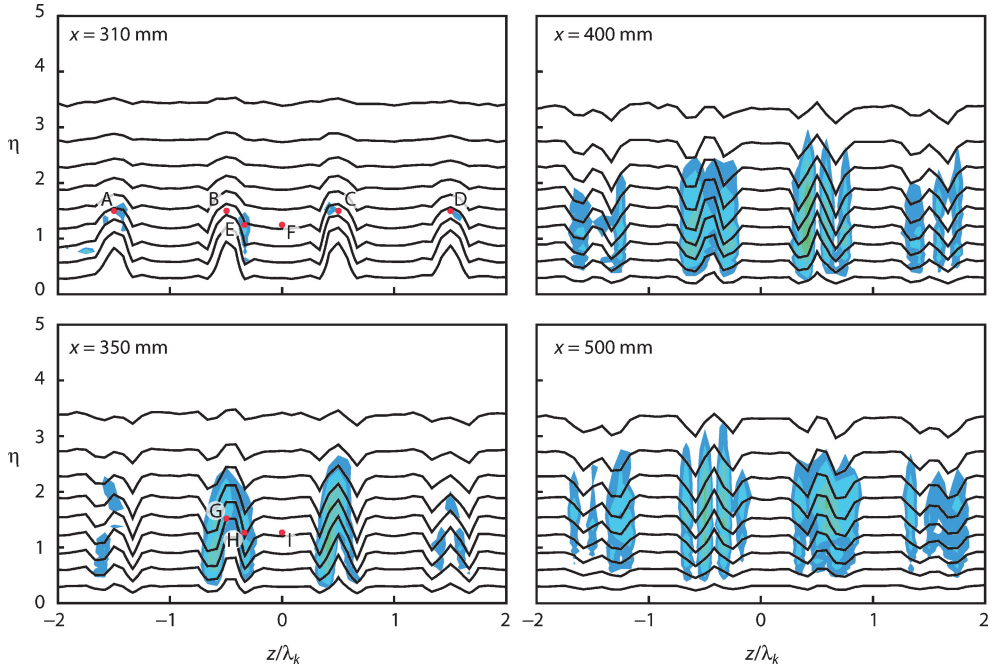

Fig. 5 Contours of u'_{rms} and U for $Re_k = 202$: black lines, 10% increments of U_∞ in U; colored contours, exponentially distributed contours of u'_{rms}; and red circles, points referred to in text.

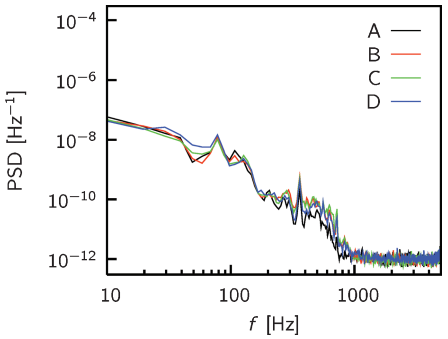

Fig. 7 Power spectra obtained at points A, B, C, and D of Fig. 5.

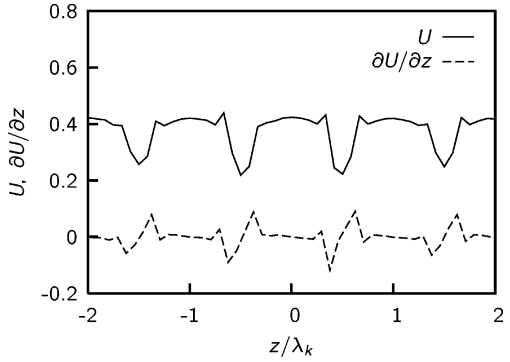

Fig. 8 Spanwise variation of U and $\partial U/\partial z$ at $x = 310$ mm and $\eta = 1.25$ for $Re_k = 202$.

$\partial^2 U/\partial \eta^2 = 0$. This can be seen in Fig. 6, where the phase-locked centerline velocity profile, U_c, the derivative of this profile, $\partial U_c/\partial \eta$, and the basic state profile are plotted at $x = 310$ mm. In Fig. 6 and subsequently, the U_c and $\partial U_c/\partial \eta$ profiles are not drawn in the region close to the surface where the velocity cannot be measured. The fact that the inflection point and the maximum u'_{rms} intensity occur at the same point indicates that the fluctuating lobes may result from a Kelvin–Helmholtz-type (KH) instability mechanism of a local shear layer in the η direction. Lobes of increased fluctuation intensity at these points will be referred to as heads. The power spectra obtained at the heads (points indicated by A, B, C, and D in Fig. 5) are compared in Fig. 7. The spectra are all quite similar, even though a lobe is not visible behind the second element at B due to the selection of the contour levels.

The fluctuation intensity behind the second roughness element located at $z/\lambda_k = -0.5$ is concentrated downstream of its right edge instead of downstream of its centerline possibly because the local shear layer in the z direction is stronger than in the other roughness wakes. Figure 8 shows U and $\partial U/\partial z$ for $\eta = 1.25$. The streamwise velocity deficits behind the roughness are clearly visible. The local inflection points in the spanwise direction ($\partial^2 U/\partial z^2 = 0$) appear exactly at the locations where the fluctuations are largest, and this indicates a possible KH instability generated by a local shear layer in the z direction. Lobes of increased fluctuation intensity at these points will be referred to as legs. Although other elements' $\partial U/\partial z$ maxima are comparable to the second element's wake, the lobe appears only in the second element's wake, at point E, because only the fluctuations near point E are greater than the the minimum contour level.

The power spectra obtained at the head and in the legs can be compared to a reference point that is not in the wake of elements. For this purpose, a point located between the elements at $\eta = 1.25$ is selected and will be referred to as the midpoint. The power spectra obtained at the head, right leg, and midpoint (points B, E, and F, respectively, in Fig. 5) are compared in Fig. 9. A band of amplified frequencies extending from 300 to 800 Hz is visible at the head and in the leg as are a few sharp peaks that may or may not be physical. Additionally, low-frequency fluctuations centered at 35 Hz are also present in the leg. As expected, the magnitudes at the midpoint are noticeably less than the magnitudes at the head and in the right leg.

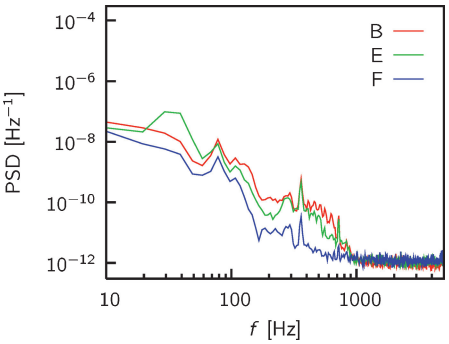

Fig. 9 Power spectra obtained at points B, E, and F of Fig. 5.

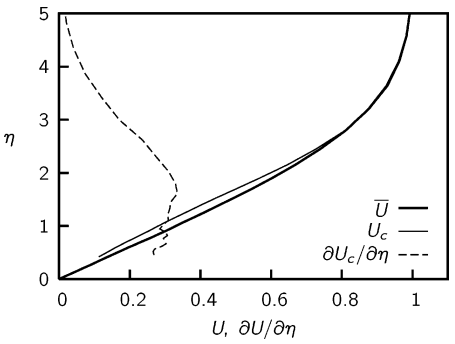

Fig. 10 Basic state, centerline, and $\partial U_c/\partial \eta$ profiles at $x = 350$ mm for $Re_k = 202$.

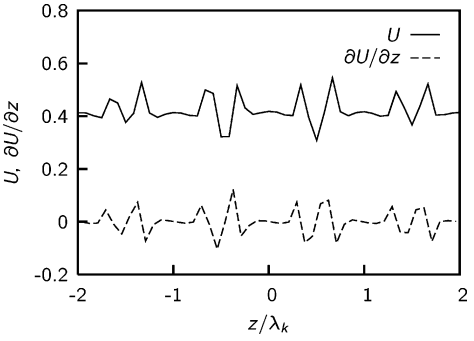

Fig. 11 Spanwise variation of U and $\partial U/\partial z$ at $x = 350$ mm and $\eta = 1.25$ for $Re_k = 202$.

Moving downstream to $x = 350$ mm, the fluctuations are stronger and cover a wider spanwise region. The lobes have evolved into inverted V-shaped structures that are roughly symmetric about the roughness elements' centerlines. This implies that the shear layers in the z direction on both sides of the element are simply parts of a complex three-dimensional shear layer that is hinted at by the Klebanoff et al.[26] data. The shear layer is in the wall-normal direction along the roughness centerline and is in the spanwise direction closer to the surface on both sides. Between these locations, the shear layer's direction gradually changes forming a curved locus of inflection points. The inverted V structures could be interpreted as elongated hairpin vortices tethered to the roughness elements on their spanwise edges. It is suspected that the locus of inflection points constitutes the axis of the unsteady hairpin vortex.

Figures 10 and 11 are equivalent to Figs. 6 and 8; they show local shear layers in the η and the z directions at $x = 350$ mm. In Fig. 10, the $\partial U_c/\partial \eta$ profile has a broad peak extending from $\eta \approx 1$ to $\eta \approx 2$. This translates into more extended fluctuation lobes in the wall-normal direction, and these are clearly visible in Fig. 5. Similar to $x = 310$ mm, the local inflection points in spanwise direction appears exactly at the location where the fluctuation intensity is maximum, reinforcing the notion that the fluctuations in the legs may be generated by a KH-type instability associated with shear in the z direction.

Figure 12 shows the power spectra obtained at the head, right leg, and the midpoint at $x = 350$ mm, points G, H, and I, respectively. Compared to Fig. 9, the power spectrum of the midpoint remains essentially unchanged, whereas the spectra at the head and the right leg show a band of amplified frequencies extending from 300 to 800 Hz, as well as a sharp peak near 360 Hz. For the experiment's conditions, TS unstable frequencies are between 100 and 200 Hz and, therefore, the observed fluctuations are not associated with the TS mechanism. To link the frequencies in the power spectra with the proposed KH instability mechanism, the local shear layer in the z direction is considered. A representative frequency for the unstable shear layer between the centerline at $\eta = 1.25$ and point H is given by $[U_c(\eta = 1.25) - U(\eta = 1.25, z_H)]/(z_H - z_c)$, approximately 750 Hz. This value is in good agreement with what is observed in the spectra of Fig. 12, and this gives additional support to the notion that the measured disturbances may be the result of a KH instability. Additionally, note that transient growth of unsteady disturbances decreases as the disturbance frequency increases[14,15] and unsteady transient disturbances, if they exist, would be at frequencies well below TS frequencies.

At $x = 400$ mm, the fluctuation intensity decreases and the structures split into as many as three lobes that cover an even larger spanwise region. It is possible that the structures split into four lobes but that two or three lobes are sometimes observed because of the measurements' spanwise resolution. At $x = 500$ mm, in the wake of the second roughness element, the u'_{rms} distribution is split into four nearly identical lobes centered at the spanwise inflection points.

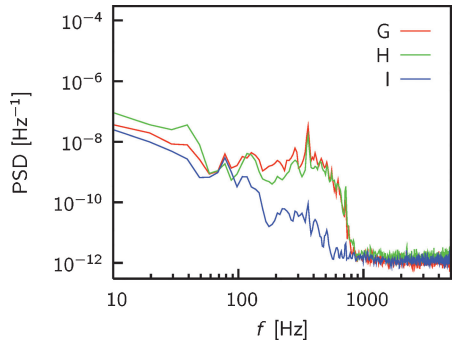

Fig. 12 Power spectra obtained at points G, H, and I of Fig. 5.

The preceding discussion for $Re_k = 202$ configuration applies as a whole to the second subcritical roughness configuration with $Re_k = 264$ except for the fact that the $Re_k = 264$ configuration produces somewhat larger fluctuation intensities. For this reason a detailed description of the $Re_k = 264$ configuration is omitted for brevity.

B. Transitional Configuration, $Re_k = 334$

Figure 13 shows the distribution and evolution of u'_{rms} for the $Re_k = 334$ configuration with the same U and u'_{rms} contour levels used in Fig. 5. It is immediately apparent that both the unsteady fluctuation intensity and the steady disturbance levels are higher than those of the baseline configuration with $Re_k = 202$ and that this roughness configuration leads to rapid transition to turbulence.

Downstream of the roughness array at $x = 310$ mm, the unsteady velocity fluctuations are concentrated in three regions, one directly above the roughness centerline around $\eta = 1.5$ and two on both sides of the roughness element. These regions are most distinct and symmetric for third and fourth elements from the left. Again, the two lobes located downstream of either side of the roughness element are associated with local shear layers in the z direction, and the lobe directly downstream of the centerline is associated with the local shear layer in the η direction. This can be seen in Figs. 14 and 15, which show the inflection points in the η and in the z directions, respectively. In Fig. 14, the inflection point in the wall-normal direction is again at $\eta = 1.5$, but $\partial U_c/\partial\eta$ is significantly larger that that of the $Re_k = 202$ configuration in Fig. 6. In Fig. 15, the streamwise

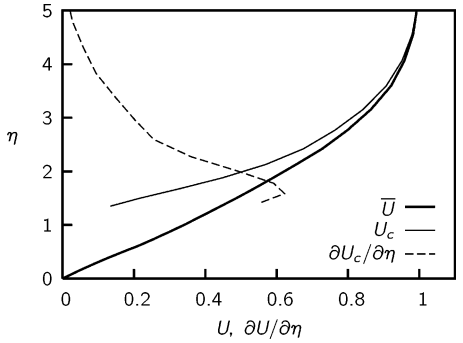

Fig. 14 Basic state, centerline, and $\partial U/\partial\eta$ profiles at $x = 310$ mm for $Re_k = 334$.

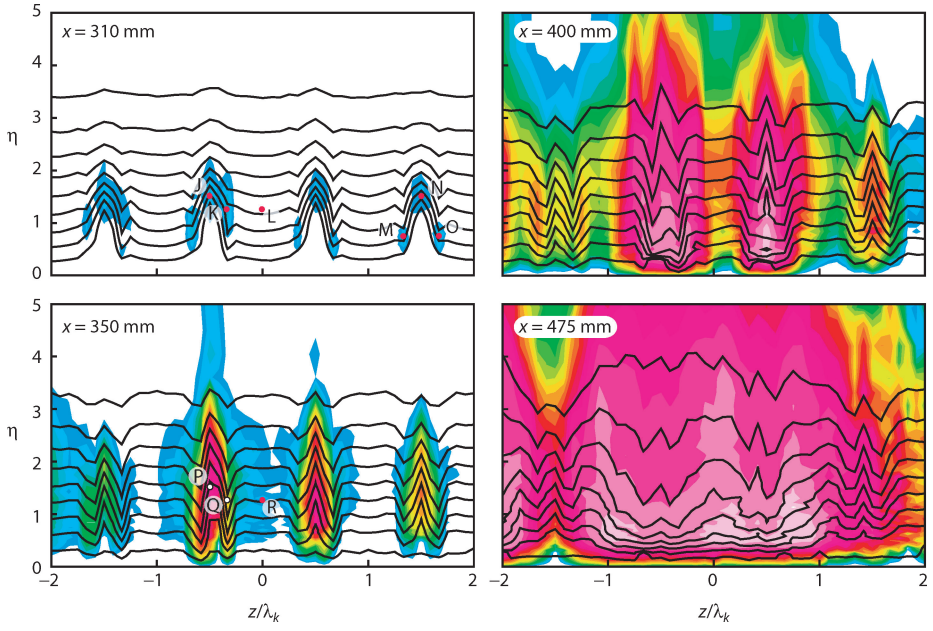

Fig. 13 Contours of u'_{rms} and U for $Re_k = 334$; all contour levels identical to Fig. 5: red and black circles, points referred to in the text.

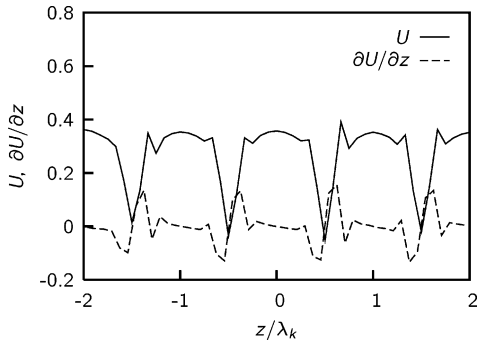

Fig. 15 Spanwise variation of U and $\partial U/\partial z$ at $x = 310$ mm and $\eta = 1.25$ for $Re_k = 334$.

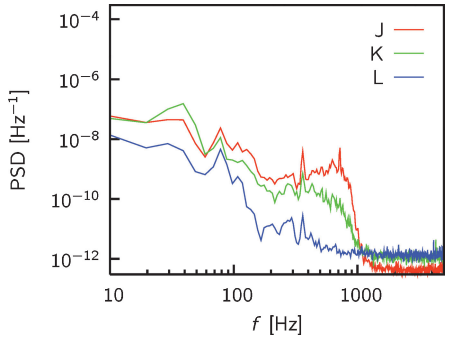

Fig. 16 Power spectra obtained at points J, K, and L of Fig. 13.

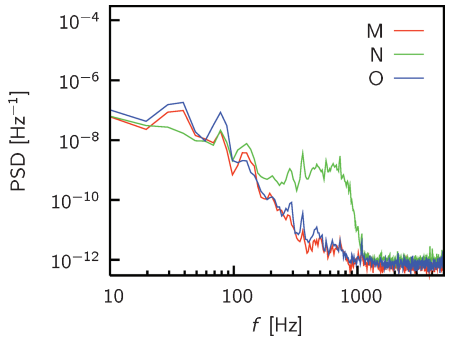

Fig. 17 Power spectra obtained at points M, N, and O of Fig. 13.

velocity deficits behind the elements are also observed to be larger than their counterparts of the baseline configuration. Again, the spanwise locations of the $\partial U/\partial z$ maxima match the spanwise locations of the legs in Fig. 13.

The power spectra obtained at the head, right leg, and midpoint (points J, K, and L, respectively, in Fig. 13) of the transitional configuration are compared in Fig. 16. These points are equivalent to points B, E, and F in Fig. 5, whose power spectra are shown in Fig. 9. As before, a broad band of amplified frequencies from 300 to 800 Hz is visible in the head and the leg. However, the fluctuation intensities in this band are higher and are shifted toward higher frequencies than those of the $Re_k = 202$ configuration.

The lobes centered around points J and K in the wake of the second roughness element in Fig. 13 are very close to one another, and the fluctuations may influence the neighboring lobe. However, the head and leg regions are distinct for the third and fourth elements from the left. In an effort to better understand the frequency distribution in each region, Fig. 17 shows the power spectra obtained at locations indicated by points M, N, and O in Fig. 13. Points M and O are located downstream of left and right legs of the rightmost roughness element, both at $\eta = 0.75$. Point N is located in the head, and the spectra at point N in Fig. 17 can be compared to that at

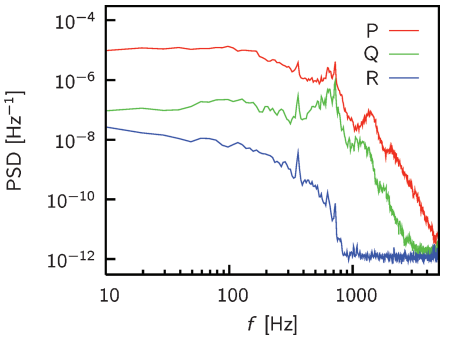

Fig. 18 Power spectra obtained at points P, Q, and R of Fig. 13.

point J in Fig. 16. As expected, the power spectra obtained in the legs, that is, at points M and O, are essentially identical as the configuration's symmetry requires. The legs contain more power in the low-frequency region around 35 Hz compared to the head at point N. On the other hand, the head's spectrum contains more power in the high-frequency region. This suggests that this frequency band originates from the top of the roughness element and is associated with the wall-normal shear layer. Conversely, the low-frequency fluctuations in the legs may be associated with the spanwise shear layer on both sides.

At $x = 350$ mm, the unsteady fluctuations are greatly intensified compared to the same streamwise location for the baseline configuration. Additionally, the region covered by the fluctuations is increased such that the second and third roughness elements' unsteady wakes are joined and the second roughness element's fluctuations reach the edge of the boundary layer. The local shear layers in the η and the z directions at $x = 350$ mm for the transitional configuration are similar to those of baseline configuration with larger amplitudes.

The power spectra obtained at the head, right leg, and midpoint for $x = 350$ mm (points P, Q, and R, respectively, in Fig. 13) are compared in Fig. 18. These points are equivalent to points G, H, and I in Fig. 5, and the power spectra can be compared to those in Fig. 12. Immediately apparent in Fig. 18 are the amplified fluctuations in almost all of the low-frequency region. The unsteady disturbance power contained in the head is larger than the power contained in the right leg, which contains more power than the midpoint. This matches with the contour levels shown in Fig. 13. The power contained at point R is noticeably higher than the midpoint L at $x = 310$ mm due to the merging of the elements' unsteady wakes. When compared to the $Re_k = 202$ configuration in Fig. 12 and $x = 310$ mm in Fig. 16, the 300–800-Hz frequency band has amplified several orders of magnitude in the transitional configuration shifting toward higher frequencies of this band. Figure 18 also shows the formation and growth of the harmonics of the broad band of amplified frequencies centered roughly at 650 Hz. The shedding frequency of 650 Hz obtained here corresponds to $Sr = 0.15$, which is consistent with a reasonable extrapolation of the Klebanoff et al. data.[26]

At $x = 400$ mm, abrupt changes occur in both the steady and unsteady disturbances. The unsteady wakes of all roughness elements shown in Fig. 13 are joined, and most of the boundary layer is contaminated by turbulent fluctuations. The mixing downstream of the middle two roughness elements is most severe, and the steady velocity contours begin to deviate from their usual laminar appearance. By $x = 475$ mm, the flow is completely contaminated by unsteady fluctuations with high-turbulence levels. The steady velocity contours are strongly affected by turbulent mixing and are well on their way toward a fully developed turbulent boundary-layer profile. The maximum u'_{rms} in Fig. 13 is 16% of U_∞.

C. Streamwise Evolution of the Unsteady Disturbance Energy

A quantitative assessment of the unsteady disturbances' evolution can be made by computing e_{rms}, the unsteady disturbance energy contained in a single roughness-array wavelength. The downstream evolution of e_{rms} generated by the roughness element at

Table 1 Spatial amplitude growth rates

	α_{650}		α_{1300}:
Re_k	$310 \le x \le 320$ mm	$320 \le x \le 340$ mm	$320 \le x \le 340$ mm
202	0.019 ± 0.002	0.015 ± 0.002	——
264	0.046 ± 0.002	0.018 ± 0.008	——
334	0.143 ± 0.022	0.045 ± 0.006	0.069 ± 0.006

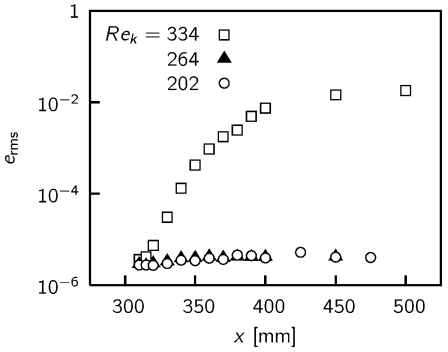

Fig. 19 Streamwise evolution of total unsteady disturbance energy e_{rms} in wake of roughness element located at $z/\lambda_k = -0.5$.

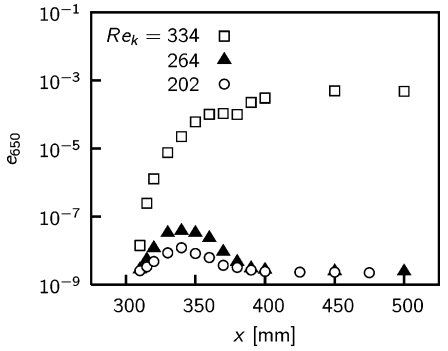

Fig. 20 Streamwise evolution of e_{650} in wake of roughness element at $z/\lambda_k = -0.5$.

$z/\lambda_k = -0.5$ is shown in Fig. 19. With increasing downstream distance, the unsteady disturbance energy barely rises above the noise floor for the $Re_k = 202$ and 264 configurations. For $Re_k = 334$, however, it experiences substantial growth and then saturation as the flow becomes turbulent.

Because there is significant energy at low frequencies, the evolution of e_{rms} does not provide detailed information on the growth of the unstable band between 300 and 800 Hz that is associated with the instability mechanism. To better understand this growth and and how it does or does not trigger breakdown, e_{650} is plotted in Fig. 20. The 600–700-Hz band represented by e_{650} is representative of the center of the broad band of amplified frequencies and is more revealing than e_{rms} because the low-frequency contributions are excluded from consideration. For the $Re_k = 202$ and 264 configurations, e_{650} grows until about $x = 340$ mm. Downstream of its maximum location, the energy decays to below the noise floor of the measurements. Higher- and lower-frequency bands reach their maximum locations somewhat downstream and upstream of $x = 340$ mm, respectively. For the $Re_k = 334$ configuration, e_{650} experiences exponential growth as it does at lower Reynolds numbers Re_k in the near wake. However, it continues to grow past the x location, where its growth ceases at lower Reynold numbers Re_k. Finally, e_{650} saturates where the flow becomes fully turbulent.

Figure 21 shows the growth of the high-frequency harmonic that is centered at 1300 Hz. This band does not contain significant energy for the $Re_k = 202$ and 264 configurations but, for the $Re_k = 3344$ configuration, e_{1300} experiences exponential growth starting at $x = 320$ mm. Similar to e_{650}, energy e_{1300} saturates once breakdown occurs.

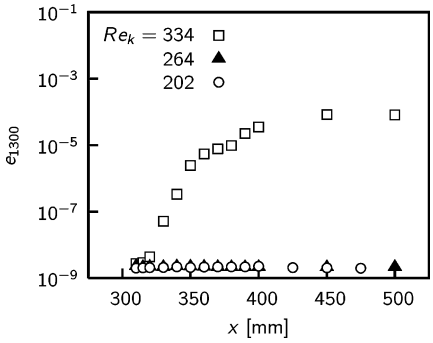

Fig. 21 Streamwise evolution of e_{1300} in wake of roughness element at $z/\lambda_k = -0.5$.

The amplitude growth rates of the two bands are given in Table 1. The growth rates α are one-half the slope of the line obtained by performing a least-squares fit to the log of e_{650} or e_{1330} across the x range indicated in Table 1. In this calculation, the streamwise length is made dimensionless using δ at x_k. In each case, the fit is performed across only three points because the growth rates decrease rapidly as x increases as is indicated by the much lower values of α_{650} between $x = 320$ and 340 mm than those between 310 and 320 mm.

When Fig. 20 is examined, it is apparent that unsteady disturbances are unstable in the roughness array's near wake for all Reynolds number Re_k values considered. Although the disturbances initially grow in the $Re_k = 202$ and 264 configurations, the entire unstable band has stabilized by about $x = 350$ mm, harmonics do not appear, and the fluctuations do not lead to transition. However, in the $Re_k = 334$ configuration, the unsteady fluctuations grow more rapidly than in the other cases, harmonics do appear, and transition results.

An explanation of the unsteady disturbances' behavior lies with the spatial evolution of the basic state provided by the roughness elements' steady wakes. It appears that the velocity deficit region behind each roughness element may support a KH-type instability and that this mechanism may be the source of the unsteady disturbances observed in each case. This would explain why the growth rates of the unsteady fluctuations increase with increasing Reynolds number Re_k: Larger velocity deficits are more unstable than smaller deficits. However, the E_{rms} data (Fig. 4) show that, in the near-wake region where unsteady fluctuations grow, the magnitude of the mean flow variations that lead to the instability are rapidly decreasing. This means that as x increases the flow becomes progressively less unstable and decreasing growth rates are observed at all Reynolds numbers Re_k in Fig. 20. However, in the transitional case, $Re_k = 334$, the initial growth rate is sufficiently large and E_{rms}, although rapidly decaying, remains sufficiently high that the unsteady fluctuations reach nonlinear amplitudes and breakdown is initiated before the basic state becomes stable to the high-frequency disturbances.

Stated another way, the critical behavior noted in the earliest experiments on transition behind three-dimensional roughness elements results from a race between unsteady fluctuation growth and the rapid relaxation of the basic state toward a spanwise-uniform Blasius flow. When $Re_k < Re_{k,\mathrm{crit}}$, the unsteady disturbances stabilize before they reach nonlinear amplitudes and decay without causing transition. However, when $Re_k > Re_{k,\mathrm{crit}}$, the unsteady disturbances are able to reach transitional amplitudes before the basic state relaxes to a condition at which they would become stable and so transition results. In this supercritical case, the two features that allow the unsteady disturbances to grow to nonlinear amplitudes are the larger initial growth rates and the longer streamwise extent of the unstable basic state.

V. Summary

Previous experiments that address transient growth have concentrated mainly on the steady disturbance field and have resolved

some important characteristics, such as the effects of roughness height and diameter on the steady disturbance energy. Because stationary transient disturbances generated by high-amplitude roughness have emerged as a promising means of suppressing TS-wave growth, the present study is intended to explore the high-amplitude limits of roughness-induced transient growth. This is achieved using an array that produces a steady disturbance field with decaying disturbance amplitudes and an unsteady disturbance field that is unstable to local variations in the mean flow. With the increase of roughness height, the initial amplitudes of the steady disturbances and the growth rates of the unsteady disturbances increase.

The spatial locations of the unsteady fluctuations correspond to local inflection points in the wall-normal and the spanwise directions, and this indicates that a KH-type instability mechanism may be responsible for the unsteady fluctuations that have previously been associated with hairpin vortices.[24,25] Frequency measurements are consistent with earlier measurements by Klebanoff et al.[26] In the near wake, fluctuation lobes along the centerline at $\eta = 1.5$ (referred to as heads) are linked to wall-normal shear and the lobes along both sides of roughness at $\eta = 1.25$ (referred to as legs) are linked to spanwise shear. Farther downstream where the fluctuations are larger, it becomes clear the the head and legs are part of the same structure that is the locus of local inflection points.

Rapid transition is observed only for $Re_k = 334$, which is in good agreement with the literature when the k/D ratio is taken into consideration.[4,9] Across all values of Reynolds number Re_k considered, unsteady disturbance growth rates increase with increasing Reynolds number Re_k. However, for the subcritical configurations, these disturbances stabilize before transition can occur. In the $Re_k = 334$ configuration, rapid transition occurs because the fluctuation growth is sufficiently large and persistent that the steady basic state cannot relax quickly enough to stable conditions to prevent transition. In this case, breakdown to turbulence is preceded by the nonlinear growth of harmonics. After the harmonics appear, the frequency spectrum quickly takes on a turbulent character and soon thereafter, the mean flow reflects the patterns of a developing turbulent boundary layer.

The utility of understanding this breakdown mechanism is that it should allow extrapolation to more complicated physical situations than the low-speed flat-plate boundary layer. Unstable but rapidly relaxing shear layers may exist in many configurations for which simple Reynolds number Re_k-based breakdown criteria have not been established or are not appropriate. Understanding breakdown as resulting from a competition between unsteady disturbance growth and steady disturbance decay permits relatively straightforward modeling that could be used to predict critical roughness features in these complicated flows.

Acknowledgments

This work was supported by the U.S. Air Force Office of Scientific Research under Grant F49620-02-1-0058 and was managed by Thomas Beutner. F. G. Ergin acknowledges Case School of Engineering for its support through a Case Prime Fellowship. The authors especially thank Donald Rizzetta and Miguel Visbal for numerous useful conversations about the experiments and their simulations.

References

[1]Goldstein, M. E., "Scattering of Acoustic Waves into Tollmien–Schlichting Waves by Small Streamwise Variations in Surface Geometry," *Journal of Fluid Mechanics*, Vol. 154, 1985, pp. 509–529.

[2]Saric, W. S., Reed, H. L., and Kerschen, E. J., "Boundary-Layer Receptivity to Freestream Disturbances," *Annual Review of Fluid Mechanics*, Vol. 34, 2002, pp. 291–319.

[3]Dryden, H. L., "Review of Published Data on the Effect of Roughness on Transition from Laminar to Turbulent Flow," *Journal of the Aeronautical Sciences*, Vol. 20, No. 7, 1953, pp. 477–482.

[4]Tani, I., "Boundary-Layer Transition," *Annual Review of Fluid Mechanics*, Vol. 1, 1969, pp. 169–196.

[5]Reshotko, E., "Transient Growth—A Factor in Bypass Transition," *Physics of Fluids*, Vol. 13, No. 5, 2001, pp. 1067–1075.

[6]Dryden, H. L., "Transition from Laminar to Turbulent Flow," *Turbulent Flows and Heat Transfer*, edited by C. C. Lin, Vol. 5, *High Speed Aerodynamics and Jet Propulsion*, Princeton Univ. Press, Princeton, NJ, 1959, pp. 3–74.

[7]Smith, A., and Clutter, D. W., "The Smallest Height of Roughness Capable of Affecting Boundary-Layer Transition," *Journal of the Aero/Space Sciences*, Vol. 26, No. 4, 1959, pp. 229–245, 256.

[8]Tani, I., "Effect of Two-Dimensional and Isolated Roughness on Laminar Flow," *Boundary Layer and Flow Control*, edited by G. V. Lachmann, Vol. 2, Pergamon, 1961, pp. 637–656.

[9]von Doenhoff, A. E., and Braslow, A. L., "The Effect of Distributed Surface Roughness on Laminar Flow," *Boundary Layer and Flow Control*, edited by G. V. Lachmann, Vol. 2, Pergamon, 1961, pp. 657–681.

[10]Sedney, R., "A Survey of the Effect of Small Protuberances on Boundary-Layer Flows," *AIAA Journal*, Vol. 11, No. 6, 1973, pp. 782–792.

[11]Schmid, P. J., and Henningson, D. S., *Stability and Transition in Shear Flows*, Springer, New York, 2001.

[12]Butler, K., and Farrell, B., "Three-Dimensional Optimal Perturbations in Viscous Shear Flow," *Physics of Fluids A*, Vol. 4, No. 8, 1992, pp. 1637–1650.

[13]Andersson, P., Berggren, M., and Henningson, D. S., "Optimal Disturbances and Bypass Transition in Boundary Layers," *Physics of Fluids*, Vol. 11, No. 1, 1999, pp. 134–150.

[14]Luchini, P., "Reynolds-Number-Independent Instability of the Boundary Layer over a Flat Surface: Optimal Perturbations," *Journal of Fluid Mechanics*, Vol. 404, 2000, pp. 289–309.

[15]Tumin, A., and Reshotko, E., "Spatial Theory of Optimal Disturbances in Boundary Layers," *Physics of Fluids*, Vol. 13, No. 7, 2001, pp. 2097–2104.

[16]White, E. B., and Reshotko, E., "Roughness-Induced Transient Growth in a Flat-Plate Boundary Layer," AIAA Paper 2002-0138, 2002.

[17]White, E. B., "Transient Growth of Stationary Disturbances in a Flat Plate Boundary Layer," *Physics of Fluids*, Vol. 14, No. 12, 2002, pp. 4429–4439.

[18]White, E. B., and Ergin, F. G., "Receptivity and Transient Growth of Roughness-Induced Disturbances," AIAA Paper 2003-4243, 2003.

[19]White, E. B., Rice, J. M., and Ergin, F. G., "Receptivity of Stationary Transient Disturbances to Surface Roughness," *Physics of Fluids*, Vol. 17, No. 6, 2005, 064109.

[20]Cossu, C., and Brandt, L., "Stabilization of Tollmien–Schlicting Waves by Finite Amplitude Optimal Streaks in the Blasius Boundary Layer," *Physics of Fluids*, Vol. 14, No. 8, 2002, pp. L57–L60.

[21]Cossu, C., and Brandt, L., "On Tollmien-Schlichting-like Waves in Streaky Boundary Layers," *European Journal of Mechanics B/Fluids*, Vol. 23, No. 6, 2004, pp. 815–833.

[22]Saric, W. S., Carrillo, R. B., Jr., and Reibert, M. S., "Nonlinear Stability and Transition in 3-D Boundary Layers," *Meccanica*, Vol. 33, No. 5, 1998, pp. 469–487.

[23]Andersson, P., Brant, L., Allessandro, B., and Henningson, D., "On the Breakdown of Boundary Layer Streaks," *Journal of Fluid Mechanics*, Vol. 428, 2001, pp. 29–60.

[24]Gregory, N., and Walker, W. S., "The Effect on Transition of Isolated Surface Excrescences in the Boundary Layer," Aeronautical Research Council, Technical Rept. R&M 2779, 1956.

[25]Acarlar, M., and Smith, C., "A Study of Hairpin Vortices in a Laminary Boundary Layer. Part 1. Hairpin Vortices Generated by a Hemisphere Protuberance," *Journal of Fluid Mechanics*, Vol. 175, 1987, pp. 1–41.

[26]Klebanoff, P., Cleveland, W., and Tidstrom, K., "On the Evolution of a Turbulent Boundary Layer Induced by a Three-Dimensional Roughness Element," *Journal of Fluid Mechanics*, Vol. 237, 1992, pp. 101–187.

[27]Klebanoff, P., Schubauer, G., and Tidstrom, K., "Measurements of the Effect of Two-Dimensional and Three-Dimensional Roughness Elements on Boundary-Layer Transition," *Journal of the Aeronautical Sciences*, Vol. 22, 1955, pp. 803–804.

[28]Tani, I., Komoda, A., Komatsu, Y., and Iuchi, M., "Boundary Layer Transition by Isolated Roughness," Aeronautical Research Inst., Technical Rept. 375, Tokyo Univ., Tokyo, 1962.

[29]Mochizuki, M., "Hot-Wire Investigations of Smoke Patterns Caused by a Spherical Roughness Element," *Natural Science Reports, Ochanomizu Univ.*, Vol. 12, No. 2, 1961, pp. 87–101.

[30]Kendall, J., "Laminar Boundary Layer Velocity Distortion by Surface Roughness: Effect upon Stability," AIAA Paper 81-0195, 1981.

[31]White, E. B., and Ergin, F. G., "Using Laminar-Flow Velocity Profiles to Locate the Wall Behind Roughness Elements," *Experiments in Fluids*, Vol. 36, No. 2, 2004, pp. 805–812.

[32]Landahl, M. T., "A Note on an Algebraic Instability of Inviscid Parallel Shear Flows," *Journal of Fluid Mechanics*, Vol. 98, 1980, pp. 243–251.

[33]Tumin, A., and Reshotko, E., "The Problem of Boundary-Layer Flow Encountering a Three-Dimensional Hump Revisited," AIAA Paper 2004-0101, 2004.

[34]Press, W. H., Teukolsky, S. A., Vetterling, W. T., and Flannery, B. P., *Numerical Recipes in C*, 2nd ed., Cambridge Univ. Press, Cambridge, England, U.K., 1992.

[35]Saric, W. S., "Low-Speed Boundary Layer Transition Experiments," *Transition: Experiments, Theory and Computation*, edited by T. C. Corke, G. Erlebacher, and M. Hussaini, Oxford Univ. Press, Oxford, 1996, pp. 1–114.

[36]Rice, J. M., *Roughness Receptivity and Scaling of Non-Optimal Transient Disturbances*, M.S. Thesis, Case Western Reserve Univ., Cleveland, OH, May 2004.

[37]Rizzetta, D. P., and Visbal, M. R., "Direct Numerical Simulations of Flow past an Array of Distributed Roughness Elements," *AIAA Journal* (submitted for publication).

D. Gaitonde
Associate Editor

Color reproductions courtesy of the Air Force Office of Scientific Research.